

# NUMERICAL METHODS FOR THE 3-DIMENSIONAL 2-BODY PROBLEM IN THE ACTION-AT-A-DISTANCE ELECTRODYNAMICS

I.N.NIKITIN\* and J. DE LUCA\*\*

\* *German National Research Center for Information Technology,  
53754 Sankt Augustin, Germany*

\*\* *Departamento de Física, Universidade Federal de São Carlos, Via Washington Luis, km 235,  
13565-905 São Carlos, SP, Brazil*

E-mail: Igor.Nikitin@gmd.de | deluca@df.ufscar.br

Received 20-03-2001

We develop two numerical methods to solve the differential equations with deviating arguments for the motion of two charges in the action-at-a-distance electrodynamics. Our first method uses Stürmer's extrapolation formula and assumes that a step of integration can be taken as a step of light ladder, which limits its use to shallow energies. The second method is an improvement of pre-existing iterative schemes, designed for stronger convergence and can be used at high-energies.

*Keywords:* numerical methods; differential equations with deviating arguments; Wheeler-Feynman electrodynamics.

## 1. Action-at-a-distance electrodynamics

In this paper we continue an investigation initiated in <sup>1</sup> and here extended to the numerical analysis of the 3-dimensional two-body problem in the relativistic action-at-a-distance electrodynamics of Wheeler and Feynman<sup>2</sup>, henceforth called 3D WF. The dynamics follows from the Schwarzschild-Tetrode-Fokker<sup>3</sup> direct-interaction functional. Equations of motion are derived from Hamilton's principle for the action integral

$$S = - \sum_i \int m_i c ds_i - \sum_{i>j} (e_i e_j / c) \int \int \delta(\|x_i - x_j\|^2) \dot{x}_i \cdot \dot{x}_j ds_i ds_j,$$

where the four-vector  $x_i(s_i)$  represents the four-position of particle  $i$  parametrized by arc-length  $s_i$ , double bars indicate four-vector modulus  $\|x_i - x_j\|^2 \equiv (x_i - x_j) \cdot (x_i - x_j)$  and the dot indicates Minkowski relativistic scalar product of four-vectors with metric tensor  $g_{\mu\nu} = \text{diag}(1, -1, -1, -1)$ . Integration is to be carried over the whole particle trajectories, at least formally <sup>4</sup>, unlike other usual additive cases of classical mechanics. The above action integral describes an interaction at the advanced and retarded light-cones with an electromagnetic potential given by half the sum of the advanced and retarded Liénard-Wiechert potentials <sup>5</sup>. Wheeler

and Feynman showed that electromagnetic phenomena can be described by this direct action-at-a-distance theory in complete agreement with Maxwell's theory as far as the classical experimental consequences<sup>2,6</sup>. This direct-interaction formulation of electrodynamics was developed to avoid the complications of divergent self-interaction, as there is no self-interaction in this theory, and also to eliminate the infinite number of field degrees of freedom of Maxwell's theory<sup>7</sup>. It was a great inspiration of Wheeler and Feynman in 1945, that followed a lead of Tetrode<sup>3</sup> and showed that with the extra hypothesis that the electron interacts with a completely absorbing universe, the advanced response of this universe to the electron's retarded field arrives *at the present time of the electron* and is equivalent to the local instantaneous self-interaction of the Lorentz-Dirac theory<sup>8</sup> plus the retarded interaction among charges<sup>10</sup>. The action-at-a-distance theory is also symmetric under time reversal, as the Fokker action includes both advanced and retarded interactions. Dissipation in this time-reversible theory is due to interaction with the other charges of the universe and becomes a matter of statistical mechanics of absorption<sup>9</sup>. The area of Wheeler-Feynman electrodynamics has been progressing slowly but steadily since 1945: quantization was achieved by use of the Feynman path integral technique and the effect of spontaneous emission was successfully described in terms of interaction with the future absorber, in agreement with quantum electrodynamics. It was also shown that it is possible to avoid the usual divergencies associated with quantum electrodynamics by use of proper cosmological boundary conditions<sup>10</sup>. As far as understanding of the dynamics governed by the equations of motion, the state of the art is as follows: the exact circular orbit solution to the attractive two-body problem was proposed in 1946 by Schonberg<sup>11</sup> and rediscovered in 1962 by Schild<sup>12</sup>. The 1-dimensional symmetric two-electron scattering is a special case where the equations of motion simplify a lot and it has been studied by many authors, both analytically and numerically<sup>13,14,15</sup>. In this very special case the initial value functional problem surprisingly requires much less than an arbitrary initial function to determine a solution manifold with the extra condition of bounded manifold for all times. It was shown that the solution is uniquely determined by the inter-electronic distance at the turning point if this distance is large enough<sup>14</sup>. As a result of this theorem, there is a single continuous parameter (the positive energy) describing the unique non-runaway P-symmetric solution at that given positive energy. Numerical analysis<sup>1</sup> shows that at some critical energy this unique solution splits into three solutions, from which two are not P-symmetric themselves, but are P-conjugated to each other.

For the 3D WF the only known result is the linear stability analysis of the Schonberg-Schild circular orbits<sup>16</sup>, exhibiting an infinite number of unstable solutions for the characteristic equation. This paradoxical linear instability of circular orbits is a warning that the first relativistic correction can not be the generic unfolding of this complex dynamics considered as a perturbation of the integrable Coulombian system. The question whether these unstable solutions are present in

the exact theory can be investigated numerically, which is a use for our integrators.

In the following we discuss three numerical methods for the solution of 3D WF. The first one, originally proposed in <sup>17</sup>, involves solving the equations with respect to the most advanced velocities and accelerations, converting the equation of motion to a double-delay form. As a result, the evolution becomes completely and quite naturally determined by the past trajectory, allowing an easy numerical implementation. However, in section 2.1 we show that this numerical scheme is largely unstable and can not be used in practice. We discuss the reasons of this instability, which are closely related to the existence of unstable solutions of the characteristic equation<sup>16</sup>. In section 2.2 we describe a method, based on usage of special parametrization of world lines (light-ladder parametrization <sup>1</sup>), which implements the direct integration of the equations when the integration step is equal to one step of light ladder. The method is applicable at low velocities  $v/c \sim 10^{-2}$  and is stable at least for integration times up to  $N \sim 10^6$  revolutions of the particles. In section 2.3 we consider an iterative method, originally proposed in <sup>13</sup> to solve the 1-dimensional 2-body WF problem, which after certain modifications can be applied to the 3-dimensional case. This method works with shorter intervals of integration than the light-ladder and it is able to resolve the structure of solutions for intervals smaller than one light ladder step and also converges at high energies. The results obtained using the methods are presented in section 3.

The mathematical structure of the equations of motion of 3D WF is described in Appendix A. Poincare's invariance of the Fokker Lagrangian implies the associated non-local Noether's constants of motion as integrals over a segment of the past history<sup>5,2,12</sup>. These conserved integrals provide a useful check for the numerical work and we discuss them as well in Appendix A. Further appendices provide necessary details about numerical schemes.

## 2. Computational methods

### 2.1. Solving the equations with respect to the advanced variables

The most intuitively attractive method, which is based on solving the equations of motion for the most advanced velocities and accelerations, turns out to be numerically unstable. The reason for this instability can be easily understood considering the simpler 1-dimensional version of the problem with repulsive potential. We henceforth use the letter  $x$  to denote the cartesian vector of position for particle 1 and the letter  $y$  to denote the position of particle 2. The velocity and acceleration evaluated at the present time of particle 1 are written as  $v_x$  and  $a_x$  respectively. An upper plus (or minus) above quantities signifies that the quantity is evaluated at the future (or past) point of the light cone starting from the present position of other particle. The equations of motion for 1-dimensional repulsive motion have

the simple form

$$a_x = \frac{1}{2}(1 - v_x^2)^{3/2} \left( \frac{1 + v_y^-}{1 - v_y^-} \cdot (y^- - x)^{-2} + \frac{1 - v_y^+}{1 + v_y^+} \cdot (y^+ - x)^{-2} \right),$$

in units  $e = m = c = 1$ . The equations for the other particle are obtained by exchanging  $x \leftrightarrow y$  in the above formula. The idea is to solve the above equation of motion of particle  $x$  for the most advanced velocity  $v_y^+$  of particle  $y$  as

$$v_y^+ = \frac{1 - G}{1 + G}, \quad G \equiv (y^+ - x)^2 \cdot \left[ \frac{2a_x}{(1 - v_x^2)^{3/2}} - \frac{1 + v_y^-}{1 - v_y^-} \cdot (y^- - x)^{-2} \right].$$

The equation for  $v_x^+$  is again obtained by interchanging  $x \leftrightarrow y$ . It is seen that we have a functional differential equation with delayed argument only, as first pointed out in<sup>17</sup>. As far as initial conditions go, the general theory on delay equations<sup>18</sup> tells us that we need to provide an initial  $C^2$  function describing the position of particle  $x$  in the past, as well as the information on particle  $y$  needed is also to be provided over twice the retardation lag seen by particle  $y$ .

The first difficulty with such setting of the problem is that the expression for  $v_y^+$  includes the *derivative*  $a_x = dv_x/dt_x$  evaluated in the retarded time. In the numerical solution this derivative should be estimated from known values  $v_x(t_x^k)$  on the integration grid using an appropriate finite difference scheme. The common feature of these schemes is that they contain a factor  $h^{-1}$ , where  $h$  is the integration step. Supposing that points  $v_x(t_x^k)$  on the grid have a computational error of order  $\epsilon$ , we will have an error in the derivative  $dv_x/dt_x$  of order  $\epsilon h^{-1}$ . Due to the functional relationship  $v_y^+ = f(dv_x/dt_x)$ ,  $v_y^+$  will have the error  $\epsilon h^{-1}$ . We see that the numerical scheme amplifies the computational error by a factor of  $h^{-1}$  after each step of light ladder. The integration step for the given equation should be small, typically  $h < 10^{-2}$ , and as a result, the scheme works only for 2-3 light ladder steps and then explodes.

The second difficulty concerns the possibility of continuation of the trajectory. It turns out that the advanced velocity given by the above expression is not guaranteed to be bounded by the velocity of light. Even in the case where numerical integration would be possible, for some initial data, at a certain point  $v_y^+$  can exceed the velocity of light and the solution cannot be continued to the next light ladder step (where this  $v_y > 1$  should enter under the square root  $(1 - v_y^2)^{1/2}$ ). At least for symmetric 1-dimensional orbits Driver's theorem<sup>14</sup> says that the set of infinitely continuable solutions is finite-dimensional, implying that for most initial functions the solution can not be continued for all times, and only a thin finite-dimensional subset of initial functions produces the good solutions. Ideally, in the given approach one should find special rare initial data, for which the solution can be continued for a large time, and this is easily seen to be a formidable numerical task.

These same difficulties plague the 2- and 3-dimensional cases, with the extra complication that the equations of motion include the advanced acceleration in a

degenerate way. An algebraic constraint appears and we solve it in Appendix B. As a result of this constraint, one component of the advanced velocity can be found from the previous acceleration (and other variables) by a functional relation of the form  $v^+ = f(a, \dots)$ . This property again makes the resulting numerical scheme unstable, like in the 1-dimensional case.

## 2.2. Direct integration scheme (low energy)

In the limit of small velocities a step of light ladder is small and can be taken as an integration step. The following computational scheme can work in this limit:

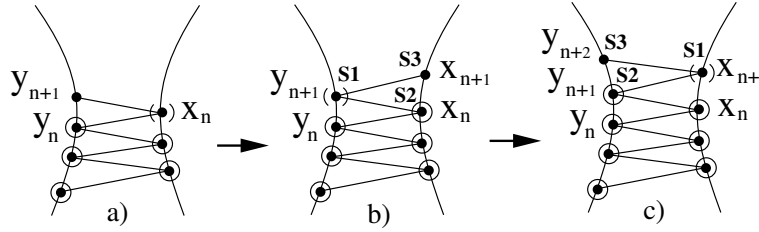


**Fig.1.** Direct integration scheme.

Suppose that coordinates and velocities are known in points  $x_k, k \leq n$ ;  $y_k, k \leq n + 1$  (shown by dots on fig.1a), and accelerations are known (stored from past integration) in points  $x_k, k \leq n - 1$ ;  $y_k, k \leq n$  (shown by circles). We then go through the following steps:

S1. Because the step of light ladder is small, we are able to compute the acceleration in point  $y_{n+1}$  as the left derivative, using a finite difference scheme, described further. This computed derivative is shown by brackets in fig.1b.

S2. As a result, we are able to find the acceleration in point  $x_n$ , using the equations of motion. This is shown in fig.1b by a circle around point  $x_n$ .

S3. We are then able to perform one integration step, applying Stürmer's method (described further), and find coordinates and velocities in point  $x_{n+1}$ .

Next we apply these three steps for  $x \leftrightarrow y$  interchanged. As a result, we have fig.1c with the same pattern of data distribution, as in fig.1a, only with shifted index  $n \rightarrow n + 1$ .

*Note:* during this process we actually have two definitions of acceleration in each point: computed by current and past velocities as left derivative (shown by brackets), and computed from the equations of motion (shown by circles). These two accelerations should coincide, and their relative difference  $|\Delta \vec{a}|/|\vec{a}|$  can be used to check the consistency of the method (see Appendix C).

**Stürmer's integration method** for the equation  $\dot{x} = f(t, x)$  is described in <sup>18</sup>,p.20. This  $n$ th order formula can be obtained from the following Taylor expansions:

$$q_k = hf(t_k, x_k),$$

$$\begin{aligned}
q_{k-1} &= q_k - \ddot{x}_k h^2 + \frac{1}{2} x_k^{(3)} h^3 - \dots + o(h^n), \\
q_{k-2} &= q_k - 2\ddot{x}_k h^2 + 2x_k^{(3)} h^3 - \dots + o(h^n), \\
q_{k-n+1} &= q_k - (n-1)\ddot{x}_k h^2 + \frac{(n-1)^2}{2} x_k^{(3)} h^3 - \dots + o(h^n),
\end{aligned} \tag{0.1}$$

by solving these  $(n-1)$  linear equations for the  $(n-1)$  unknowns  $x_k^{(p)} h^p$  and substituting them into the Taylor series for  $x_{k+1}$

$$x_{k+1} = x_k + q_k + \frac{1}{2} \ddot{x}_k h^2 + \frac{1}{6} x_k^{(3)} h^3 + \dots + o(h^n).$$

Particularly, for  $n = 8$  we have

$$\begin{aligned}
x_{k+1} &= x_k + q_k + \frac{1}{2} \Delta q_{k-1} + \frac{5}{12} \Delta^2 q_{k-2} + \frac{3}{8} \Delta^3 q_{k-3} + \frac{251}{720} \Delta^4 q_{k-4} \\
&+ \frac{95}{288} \Delta^5 q_{k-5} + \frac{19087}{60480} \Delta^6 q_{k-6} + \frac{5257}{17280} \Delta^7 q_{k-7} + o(h^8),
\end{aligned} \tag{0.2}$$

where  $\Delta^p q_k$  are defined recurrently as

$$\Delta q_{k-1} = q_k - q_{k-1}, \quad \Delta^p q_{k-1} = \Delta^{p-1} q_k - \Delta^{p-1} q_{k-1}.$$

The second derivative  $\ddot{x}_k$ , found from (0.1) at  $n = 8$ , is given by the following backward differentiation formula:

$$\ddot{x}_k = h^{-2} \sum_{p=1}^7 \frac{1}{p} \Delta^p q_{k-p} + o(h^6) \tag{0.3}$$

*Notes:*

1. The advantage of Stürmer's method is that the right hand sides of the equations do not need to be estimated in the intermediate points of the grid  $x_k$ , as for example with the type of Runge-Kutta methods, thus the necessity of interpolation of data between integration points is avoided.
2. Usage of lower order scheme reduces the precision of integration, but improves stability of the method. Particularly, the reduction of order  $n = 8 \rightarrow n = 4$ , correspondingly reduces the precision of conservation of Noether's integrals (see appendices), and increases the upper velocity, for which the method is convergent  $v = 0.006 \rightarrow v = 0.02$ .

### 2.3. Iterative scheme (high energy)

The following scheme, originally applied in <sup>13</sup> to solve the 1D WF with repulsive interaction, is here improved and implemented to integrate the 3D WF in the highly relativistic limit. The method works as follows:

An initial trajectory is guessed for the two particles, which is called iteration number zero. We then use the equations of motion to evaluate the present force caused by the past data points  $x^-, y^-$ , located on current trajectory, and future data points  $x^+, y^+$ , taken on the trajectory of previous iteration. This acceleration is used as a force field to integrate the trajectory, producing the next iterated trajectory. Repeating such integration of trajectories for fixed data on the initial segment, we arrive (if the iterations converge) to a solution of the WF problem for the initial data. As mentioned in <sup>13</sup>, this scheme is not guaranteed to be convergent, and we developed special methods of stabilization (see Appendix C), that is able to keep convergence up to very high values of the velocity.

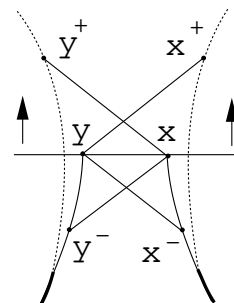


**Fig.2.** Iterative scheme.

We start our iterations from the analytically known circular solutions<sup>12</sup>, fixing the initial segments of trajectories  $\tau \in [0, 0.5]$  to arcs of circular orbits through all iterations. Then, to obtain non-circular orbits, we apply short pulses of external force to both particles immediately after the segment of initial setting. The method allows to subdivide each light ladder step into a large number of integration steps of sufficiently small size to have the correct integration at high energies. Stürmer's method, described in the previous section, can be used for integration. Special boundary conditions should be used at the end of integration interval, where no information is available about the advanced Lorentz force. These and further details about the method can be found in Appendix C.

This iterative method requires storage of the complete integrated evolution from the current and previous iterations. Due to memory restrictions, only a short part of the trajectories (up to 10 revolutions) can be determined by this method. Nevertheless, the method can provide useful information about structure of solutions at high energy when only short term evolution is needed.

### 3. Results

The computational methods, described in the previous sections, are applicable to arbitrary masses and charges. However, the case of equal masses possesses additional symmetries, and here we present the results obtained for equal masses and opposite charges (positronium-like system). Following Andersen and von Baeyer <sup>16</sup> we fix the unit system to  $c = 1$ ,  $e_x = -e_y = 1$ ,  $m_x = m_y = 2$ , so that reduced mass  $m = (m_x^{-1} + m_y^{-1})^{-1} = 1$ . We present the evolution of the system in the center-of-mass frame (CMF), using Schild's definition of CMF origin, given by Eq.(2.13) in<sup>12</sup>.

**Low energy: Darwin's precession.** At low energy the solution looks like very slowly precessing ellipse, shown on fig.3a. Between each two consequential ellipses of this figure 500 intermediate ellipses are not shown. The figure presents two coincident curves: trajectory of particle  $x$  and trajectory of particle  $y$ , reflected about the origin in CMF, demonstrating the P-symmetry of the solution.

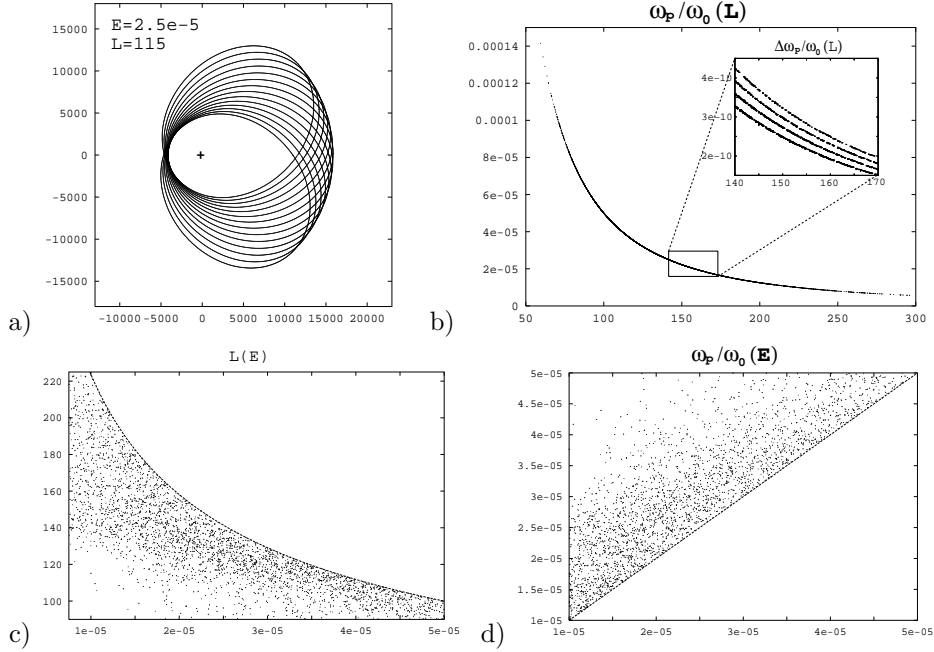


**Fig.3.** Low-energy solutions: a) trajectories, b-d) related parameters.

**Related parameters**  $(E, L, \omega_0, \omega_p)$ : binding energy  $E = 2m - \sqrt{P^2}$ , angular momentum in the CMF, angular frequencies of rotation and precession. For 10,000 solutions generated by the methods described in Appendix C, we measure these four parameters, and analyze the 4-dimensional scatter plot. Figures 3c,d represent projections of the scatter plot onto planes  $(E, L)$  and  $(E, \omega_p/\omega_0)$ . The boundary curves on these figures correspond to the circular orbit limit, and are given by formulae Eqs.(3.4),(3.5) in <sup>12</sup> and Fig.4, Eq.(5.1) in <sup>16</sup>, which for the case of equal masses and low velocities reduces to  $E = 1/(2L^2) = \omega_p/\omega_0$ .

Figure 3b represents a diagram  $(L, \omega_p/\omega_0)$ , where the scatter plot is projected almost to a curve. It shows that the ratio  $\omega_p/\omega_0$  depends mainly on  $L$  as  $\omega_p/\omega_0 = 1/(2L^2)$ . This dependence was predicted by Darwin <sup>19</sup>, who first studied the lowest order relativistic corrections to the Coulomb problem and found the described effect of precession. Using non-perturbative methods, we detect deviations from Darwin's law by an order  $10^{-10}$ , still resolvable by our measurement (which gives absolute precision of  $\omega_p/\omega_0$  about  $10^{-14}$ ). Inner image shows the difference  $\Delta\omega_p/\omega_0 = 1/(2L^2) - \omega_p/\omega_0$  versus  $L$ , for 4 narrow bands  $2EL^2 = [0.98, 1], [0.78, 0.8], [0.58, 0.6], [0.38, 0.4]$ ,



following on the image in the order down-up. Thus,  $\omega_p/\omega_0$  depends mainly on  $L$  and very weakly on  $E$ .

The structure of the graphs shows that the scatter plot in 4-dimensional space  $(E, L, \omega_0, \omega_p)$  is located on a 2-dimensional surface, like in the non-relativistic Coulombian problem, where  $(E, L)$  are the only parameters, defining the shape of solutions in the CMF. Another similarity with Coulombian problem is that the trajectories in CMF with high precision\* belong to a plane, perpendicular to the vector of angular momentum  $\vec{L}$ , even if initial data in laboratory frame are non-planar. In relativistic 3D WF problem we cannot prove planarity of orbits so easily as in Coulombian problem, and currently we have it only as a result of numerical experiment.

**High energy: Bifurcations.** Figure 4 shows pieces of the high-energetic trajectories, found by method sec.2.3. Here we again superpose trajectories  $x$  and  $(-y)$  to test the P-symmetry of the solution. On the left image a small asymmetry is visible at the beginning of the trajectories, caused by the asymmetrical statement of the problem at the beginning (see Appendix C), which exponentially disappears in the inner regions of the trajectories. When the energy increases, the asymmetry penetrates deeper to inner parts of the trajectory, and at high energy the solution completely loses the symmetry.

We define the measure of asymmetry as  $\eta = \max|\vec{x}(t) + \vec{y}(t)|$  in CMF, where the maximum is taken over a step of light ladder. Then we draw graphs  $\eta^2(E)$  for consequential light ladder steps – they are given by curves with points on the left graph of fig.5. We see that at low energies the asymmetry tends to zero with increasing number of light ladder steps, while at high energies the asymmetry tends to a non-zero value. The limiting  $\eta^2$  is well described by a linear function of  $E$  (corresponding to a supercritical pitchfork-type bifurcation  $\eta \sim \sqrt{E - E_0}$ ), it is shown by upper straight line on the graph. Lower straight lines correspond to analogously constructed dependencies for smaller asymmetry of initial conditions. Right image presents the result of assembling all pictures to 3D graph. On this graph  $\Delta L(E) = L(E) - L_0(E)$ ,  $L_0(E)$  is angular momentum for circular orbits. Line AB subdivides the diagram onto two parts: *symmetric phase* – on the left from AB the trajectories possess P-symmetry and the shape of solution is uniquely defined by two parameters  $(E, L)$ ; *asymmetric phase* – on the right from AB the symmetry is violated and given  $(E, L)$  correspond to a continuous set of solutions, differing by measure of asymmetry.

Such a structure of the phase space was actually predicted by Andersen and von Baeyer<sup>16</sup>, from the linear stability analysis of the circular orbits in 2D WF.

---

\*Motion along  $\vec{L}$ -axis consists of small oscillations with amplitude  $\Delta z = 10^{-8}$  of classical radius or relative value  $\Delta z/(XY\text{-size of orbit}) = 10^{-12}$ ; and slow Brownian motion with the velocity about  $v = 10^{-17}$ ; both motions have the same order as non-conservation of Noether's integrals, appearing due to computational errors.

This work shows that at velocities of about  $v = 0.95$ , new real eigenvalues of the characteristic equation appear, representing new degrees of freedom in the system. Corresponding linear mode, denoted by Andersen and von Baeyer as  $D^{(-)}$ , violates the P-symmetry. In our non-perturbative approach we detect this effect in the region of energy  $E \in [2.6, 2.8]$ , which for circular orbits corresponds to the region of velocities  $v \in [0.937, 0.954]$ , in good agreement with the predictions<sup>16</sup>. Actually, in point B, where the orbits are close to circular, we have  $E = 2.75$ ,  $v = 0.950$ , i.e. exact coincidence.

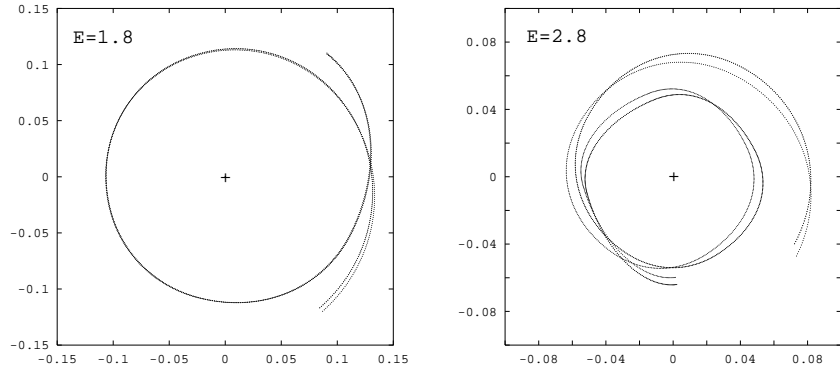


**Fig.4.** High-energy solutions: trajectories.

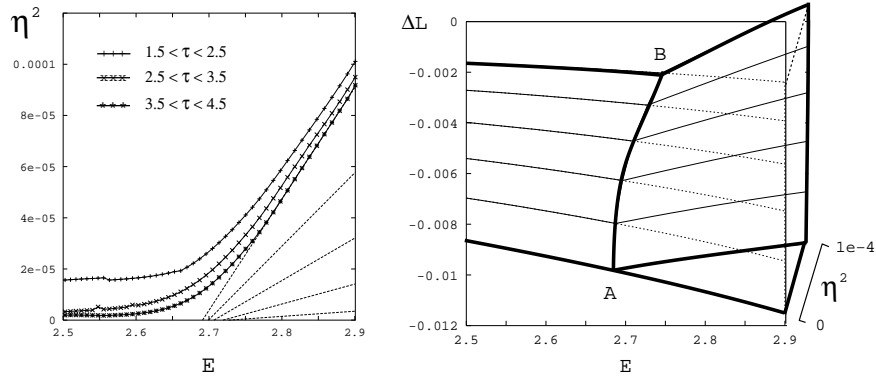


**Fig.5.** High-energy solutions: related parameters.

**Conclusion.** Two numerical methods are developed to solve 3D WF problem in the shallow and high energy ranges. The methods go further than pre-existing ones<sup>16,19</sup>, based on first order perturbation theory. Our non-perturbative analysis reproduces part of the pre-existing results with the exception of the divergent modes predicted in<sup>16</sup>, whose exponential increase violates the limitations of the linear perturbation theory<sup>16</sup>. The question about their existence in the complete theory is open. Our numerical methods do not reproduce such solutions as far as the unforced

equations of motion are considered. On the other hand, some traces of divergent modes are present in the solution of forced equations, describing the reaction to an external perturbation. The results of this analysis can be found in <sup>23</sup> and will be published elsewhere.

**Acknowledgments.** We would like to thank Dr. Martin Göbel for the warm hospitality in GMD.IMK.VE, where this article was completed, and a grant from FAPESP that supported one of us in Germany (J. De Luca).

### Appendix A: equations of motion and conserved quantities

1. The equations of motion for the 3D WF have the following form:

$$\begin{aligned} \vec{a}_x^{(\pm)} &= \frac{e_x}{m_x} \sqrt{1 - v_x^2} \left( \vec{E}_x^{\pm} \left( 1 - \frac{(\vec{r}_x^{\pm} \vec{v}_x)}{r_{x0}^{\pm}} \right) + (\vec{E}_x^{\pm} \vec{v}_x) \left( \frac{\vec{r}_x^{\pm}}{r_{x0}^{\pm}} - \vec{v}_x \right) \right), \\ \vec{E}_x^{\pm} &= \frac{(\mp) e_y}{(r_{x0}^{\pm} - (\vec{r}_x^{\pm} \vec{v}_y^{\pm}))^3} ((1 - (v_y^{\pm})^2 - (\vec{r}_x^{\pm} \vec{a}_y^{\pm})) (\vec{r}_x^{\pm} - r_{x0}^{\pm} \vec{v}_y^{\pm}) + (r_{x0}^{\pm} - (\vec{r}_x^{\pm} \vec{v}_y^{\pm})) r_{x0}^{\pm} \vec{a}_y^{\pm}), \\ \vec{r}_x^{\pm} &= \vec{y}^{\pm} - \vec{x}, \quad r_{x0}^{\pm} = \pm |\vec{r}_x^{\pm}|, \quad \vec{a}_x = \frac{1}{2} (\vec{a}_x^{(+)} + \vec{a}_x^{(-)}) + \frac{1}{m_x} \sqrt{1 - v_x^2} (\vec{F}_{ext} - (\vec{F}_{ext} \vec{v}_x) \vec{v}_x). \end{aligned} \quad (0.4)$$

Here  $\vec{a}_x$  denotes the acceleration of particle  $x$ ; variables  $\vec{E}_x^{\pm}$  are advanced and retarded components of electric field, created by particle  $y$  at the location of particle  $x$ ; variables  $\vec{y}^{\pm}, \vec{v}_y^{\pm}, \vec{a}_y^{\pm}$  stand correspondingly for position, velocity and acceleration of particle  $y$  at time moments, where the world line of particle  $y$  is intersected by the light cone with origin in  $x$ . Equations of motion for particle  $y$  are given by replacement ( $x \leftrightarrow y$ ) in these expressions. The term  $\vec{F}_{ext}$  corresponds to the force of external perturbation, used to produce perturbed initial conditions starting from the exact circular solution. For the external force we choose a cap-like form  $\vec{F}_{ext}(t) = F_a \exp[(1 - (\Delta t / (t - t_0))^2)^{-1}]$ , if  $|t - t_0| < \Delta t$ ; otherwise 0. This function is infinitely differentiable and has a finite support.

2. In our approach the equations of motion are integrated in the light ladder parametrization, which was introduced in <sup>1</sup> and modified by us in the following way: On the initial segments of the world lines, shown in bold on fig.6, we select arbitrary monotonous parametrization  $\tau \in [0, 0.5]$ , e.g. taking  $\tau$  as a linear function of the time components  $x_0, y_0$ . We then consider light rays, which consequentially reflect between the world lines, and distribute the parametrization along these rays, adding  $\tau \rightarrow \tau + 0.5$  at the points of reflection<sup>†</sup>. In this parametrization  $x(\tau)$  and  $y(\tau \pm 0.5)$  are related by light rays, so that deviation of the argument in the equations of motion becomes constant. As a result, while determining the intersection of the light cone with a world line, we are taking the data directly from one of the past integration points, not solving the equation of intersection and not performing high order interpolations of data between integration points.

Using the light ladder parametrization, we consider the evolution of the variables  $\vec{x}(\tau), \vec{y}(\tau), x_0(\tau), y_0(\tau)$  reformulating the equations of motion in terms of  $\dot{\vec{x}} = \dot{x}_0 \vec{v}_x, \dot{\vec{v}}_x = \dot{x}_0 \vec{a}_x$ , and the analogous pair for the other particle  $y$ . We substitute for  $\dot{x}_0$  a formula  $\dot{x}_0 = \dot{y}_0^- (|\vec{r}_x^-| + (\vec{r}_x^- \vec{v}_y^-)) / (|\vec{r}_x^-| + (\vec{r}_x^- \vec{v}_x))$ , which follows from differentiation of the light cone condition  $r_{x\mu}^- dr_{x\mu}^- = 0$  and expresses  $\dot{x}_0$  in terms of the past variables  $(\vec{y}^-, \vec{v}_y^-, \dot{y}_0^-)$  and current variables  $(\vec{x}, \vec{v}_x)$ . For  $\vec{a}_x$  we substitute

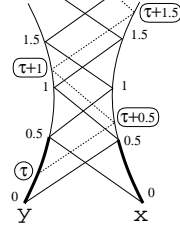


**Fig.6.** Light ladder parametrization.

<sup>†</sup>This procedure gives a  $C^\infty$ -parametrization under special conditions in the vicinity of the point  $\tau = 0.5$ , which are satisfied particularly when the initial segments of the trajectories are set to circular orbits.

the equations of motion given above (variable  $\vec{a}_y^-$ , participating in r.h.s. of the equations, is taken from the stored past history, while  $\vec{a}_y^+$  is taken in the iterative scheme of sec.2.3 from the trajectory of the previous iteration and in the direct integration scheme of sec.2.2 as  $\vec{a}_y = \dot{\vec{v}}_y/\dot{y}_0$ , where  $\dot{\vec{v}}_y$  is defined by backward differentiation formula). After these substitutions, we have a closed system of differential-difference equations for  $\vec{x}(\tau), \vec{y}(\tau)$ . Variables  $x_0(\tau), y_0(\tau)$  do not participate in the equations, and can be determined by known solution of differential-difference equations using recurrent formulae  $x_0 = y_0^- + |\vec{y}^- - \vec{x}|$ ,  $y_0 = x_0^- + |\vec{x}^- - \vec{y}|$ .

3. The conserved quantities – Noether's integrals of motion, given by Eq.(2.9-10) in <sup>12</sup>, after partial integration can be written in the following form:

$$\begin{aligned} P_\mu &= P_\mu^{(x)} + P_\mu^{(y)}, \quad P_\mu^{(x)} = m_x \frac{\dot{x}_\mu}{\sqrt{\dot{x}^2}} + \frac{e_x}{2} A_\mu^-(x) \\ &+ \frac{e_y}{2} A_\mu^+(y^-) - \frac{1}{2} (A^-(x) A^+(y^-)) (x - y)_\mu \\ &- G_\mu^{(x)}(x) + G_\mu^{(y)}(y^-), \quad P_\mu^{(y)} = (x \leftrightarrow y), \\ G_\mu^{(x)}(\xi) &= \frac{e_x}{2} \int_0^\xi d\tau_x \dot{x}_\nu F_{\nu\mu}^+(x), \quad G_\mu^{(y)}(\xi) = (x \leftrightarrow y). \end{aligned}$$

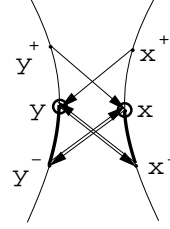


**Fig.7.** Definition of Noether's integrals.

Here  $A_\mu(\xi)$  everywhere means vector-potential *felt* in point  $(\xi)$ . For example,  $A_\mu^\pm(x)$  are the advanced and the retarded components of Lienard-Wierchert potential, created by particle  $y$ , felt in point  $x$ . The explicit formula for the potentials:  $A_\mu^\pm(x) = \pm e_y \dot{y}_\mu^\pm / (r_{x^\pm y^\pm}^\pm)$ . Analogously,  $F_{\mu\nu}^\pm(x)$  is the field tensor, created by particle  $y$ , felt in point  $x$ , given by formula  $F_{\mu\nu}^\pm(x) = \partial A_{[\mu}^\pm(x) / \partial x_{\nu]}$ , where square brackets denote antisymmetrization of indices. The above defined  $G$ -functions are equal to the integrated advanced Lorentz forces, acting on particles  $x$  and  $y$ . Using the fact that a sum of advanced and retarded Lorentz forces after integration give a local expression (change of momentum),  $G$ -terms can be rewritten to various equivalent forms, *however* it is not possible to reduce them completely to a local form (integrals cannot be eliminated). In our numerical scheme the  $G$ -integrals are computed in parallel with the main integration processes, by the same high order scheme. The given expression for Noether's integrals is graphically displayed by a diagram fig.7, where the circles mean  $m_{x,y}$ -terms, solid lines are the segments of integration in  $G$ -terms, and arrows denote potentials  $A^\pm$  (directed from source to destination).

This representation has an important difference from the Noether's integrals of the non-relativistic case (Galilean): The total momentum is composed of two contributions  $P_\mu^{(x)}$  and  $P_\mu^{(y)}$ , where  $P_\mu^{(x)}$  depends on the position of the triple of points  $(y^- x y^+)$  and  $P_\mu^{(y)}$  depends on the triple  $(x^- y x^+)$ . These triples *are independent*, as a result, both contributions are conserved separately:  $P_\mu^{(x)} = Const$ ,  $P_\mu^{(y)} = Const$ . It's easy to check that differentiation of  $P_\mu^{(x,y)}$  gives separate equations of motion for particles  $x$  and  $y$ .

The expression for the angular momentum tensor also consists of two separately conserved contributions  $L_{\mu\nu} = L_{\mu\nu}^{(x)} + L_{\mu\nu}^{(y)}$ :

$$\begin{aligned} L_{\mu\nu}^{(x)} &= x_{[\mu} V_{\nu]}^{(x)} + \frac{e_y}{2} y_{[\mu}^- A_{\nu]}^+(y^-) - G_{\mu\nu}^{(x)}(x) + G_{\mu\nu}^{(y)}(y^-), \quad L_{\mu\nu}^{(y)} = (x \leftrightarrow y), \\ V_\nu^{(x)} &= m_x \frac{\dot{x}_\nu}{\sqrt{\dot{x}^2}} + \frac{e_x}{2} A_\nu^-(x) + \frac{1}{2} (A^-(x) A^+(y^-)) y_\nu^-, \quad V_\nu^{(y)} = (x \leftrightarrow y), \\ G_{\mu\nu}^{(x)}(\xi) &= \frac{e_x}{2} \int_0^\xi d\tau_x \dot{x}_\rho x_{[\mu} F_{\rho\nu]}^+(x), \quad G_{\mu\nu}^{(y)}(\xi) = (x \leftrightarrow y). \end{aligned}$$

The above defined Noether's integrals are used to define the center-of-mass frame (CMF). Particularly,  $L_{\mu\nu}$  defines the world line of CMF origin by Eq.(2.13) in <sup>12</sup>:  $c_\mu(\lambda) = L_{\mu\nu} P_\nu / P^2 + \lambda P_\mu$ . In the coordinate system where the time axis is directed along this line and the origin is located on this line with  $c_i = 0$ , three components of the angular momentum tensor form the angular momentum vector:  $\vec{L} = (L_{23}, L_{31}, L_{12})$  and the other three components vanish:  $L_{0i} = 0$ .

Check of this property, as well as conservation of Noether's integrals were used to control the precision of numerical analysis (see Appendix C).

## Appendix B: Solving the equations of motion with respect to the most advanced variables

1. From equation (0.4) we see that the advanced contribution to the acceleration  $\vec{a}_x$  is linear on the electric field  $\vec{E}_x^+$ :

$$a_{xi}^{(+)} = A_{ij}E_{xj}^+, \quad A_{ij}(y^+; x, v_x) = \frac{e_x}{m_x} (1 - v_x^2)^{1/2} ((1 - nv_x)\delta_{ij} + (n_i - v_{xi})v_{xj}),$$

where  $\vec{n} = \vec{r}_x^+ / |\vec{r}_x^+|$ ,  $\vec{r}_x^+ = \vec{y}^+ - \vec{x}$ . An analogous expression can be written for  $\vec{a}_x^{(-)}$ . It is possible to prove that matrix  $A$  is non-degenerate, and that  $\vec{E}_x^+$  can be unambiguously found as  $\vec{E}_x^+ = A^{-1}\vec{a}_x^{(+)}$ . Taking  $\vec{a}_x^{(+)} = 2\vec{a}_x - \vec{a}_x^{(-)}$ , we finally express  $\vec{E}_x^+$  as a function of the "future" variable  $y^+$ ; present variables  $x, v_x, a_x$  and past variables  $y^-, v_y^-, a_y^-$ .

2. According to (0.4), the electric field  $\vec{E}_x^+$  depends on the position of the source  $y^+$ , its velocity  $v_y^+$  and its acceleration  $a_y^+$ , and has the following cartesian components:

$$E_{xi}^+ = \frac{-e_y}{r_{x0}^+(1 - nv_y^+)^3} \left[ \frac{1 - (v_y^+)^2}{r_{x0}^+} (n - v_y^+)_i + \underbrace{((1 - nv_y^+)\delta_{ij} - (n - v_y^+)_i n_j)}_{B_{ij}} a_{yj}^+ \right]$$

Matrix  $B$  is degenerate, i.e.  $n_i B_{ij} = B_{ij} (n - v_y^+)_j = 0$ . In order to solve this degenerate linear system with respect to  $a_y^+$ , we have to comply with the following:

a) condition of consistency (constraint found multiplying the system by  $n_i$ ):

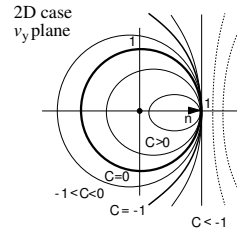
$$\underbrace{\frac{r_{x0}^+}{-e_y} (E_x^+ n)}_C = \frac{1 - (v_y^+)^2}{(1 - nv_y^+)^2} \quad (0.5)$$

b) When this condition is satisfied, the solution can be written as

$$\vec{a}_y^+ = -\frac{r_{x0}^+}{e_y} (1 - nv_y^+)^2 \vec{E}_x^+ + \lambda (\vec{n} - \vec{v}_y^+) \quad (0.6)$$

where  $\lambda$  is a so far arbitrary parameter. In the 2-dimensional case, equation  $(1 - (v_y^+)^2)/(1 - nv_y^+)^2 = C$  with  $C > 0$  defines an ellipses lying inside the circle  $(v_y^+)^2 < 1$ ; and with  $C < 0$  - ellipses ( $-1 < C < 0$ ), parabola ( $C = -1$ ) and hyperbolas ( $C < -1$ ), lying outside this circle. The physical region corresponds to  $C > 0$ , which means  $|\vec{v}_y^+| < 1$ . The consequence of the above is that it is impossible to solve uniquely for the advanced accelerations  $a_y^+$  from the equations of motion. Instead, we find a one-parameter degenerate solution plus one constraint: equation (0.5) imposed on the velocity. In the following<sup>23</sup> we choose a convenient set of variables to resolve the constraint and make the system available for explicit integration, then perform the integration using an adaptive delay equations integrator<sup>22</sup>. In the result we find instability described in section 2.1.

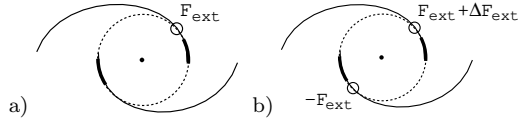
Fig.8. Algebraic constraint.



## Appendix C: Details on the statement of the numerical experiments

1. In the direct integration scheme the initial segments of trajectories were set to circular orbits<sup>12</sup>. This setting made in one half of one ladder step  $\tau \in [0, 0.5]$  is sufficient to define the further motion. However, using Stürmer's method of integration, we need also to initialize the finite differences  $\Delta^p q_k$ . Due to this reason we are setting initial segments of trajectories to circular orbits on longer intervals (up to 8 integration steps). After this setting the integrator recovers the correct circular motion. To consider non-circular orbits, at a short time after the initial setting we apply to one particle a local external force  $F_{ext}$ . As a result of this action, the system acquires non-zero total momentum and starts to move away from the origin. We then transform back to CMF and observe the evolution there.

**Fig.9.** Initial segment of trajectory: a) in direct integration scheme; b) in iterative scheme.



Using Stürmer's formulae of 8th order (0.2) and the corresponding backward differentiation formula (0.3), we have the acceleration, estimated with a precision of  $o(h^6)$ . The right hand side of the differential equations  $f(t_k, x_k, \dots)$  are dependent on the computed acceleration, and it also has precision  $o(h^6)$ . As a result, in the 8th order Stürmer's formula:  $x_{k+1} = x_k + hf_k + \dots + o(h^8)$  the last term ( $\Delta^7 q_{k-7} \sim h^8$ ) becomes ineffective, actually the method has 7th order. However, the term  $\Delta^7 q_{k-7}$  should be in any case computed to find the acceleration and can be preserved in this formula. Note also, that the acceleration terms in the Lorentz force are suppressed by additional small factor  $e^2/mr = r_0/r$  (ratio of classical radius to particles separation) so that true precision of the method is between  $o(h^8)$  and  $o((r_0/r)h^7)$ .

Using the grid of the light ladder parameter  $\tau = n \in \mathbf{Z}$ , we still have convergent scheme, until the higher order differences  $\Delta^k q_{n-k}$  are small. Actually, the role of parameter  $h$  here is played by retardation angle  $\theta \sim v/c$ . Near circular orbits we have an estimation  $r_0/r \sim (v/c)^2$ , so that for  $v/c \sim 10^{-2}$  the application of 8th order scheme gives the error of order  $10^{-16}$ , on the level of machine double precision.

The integration process can be considerably accelerated by means of *caching* of previously computed data. For this purpose we store a short buffer of past data (8 integration steps), including all variables, whose evolution is tracked, as well as the computed right hand sides of the equations of motion  $q_k$ , their finite differences  $\Delta^p q_k$  and some auxiliary variables (such as  $r_{x,y}^\pm$ , which due to relations  $r_x^\pm(\tau) = -r_y^\mp(\tau \pm 0.5)$  enter in computation several times). The content of the buffer is periodically written to a file to allow restarting of the program from previous states. To transform the system to CMF we perform a Lorentz transformation of all variables in the buffer (some of these variables, e.g. accelerations, have non-linear transformation laws).

Control of the precision was performed by comparing two definitions of acceleration (variable  $\Delta \vec{a}$  in sec.2.2) and testing the conservation of Noether's integrals (Appendix A). The relative difference  $|\Delta \vec{a}|/|\vec{a}|$  was  $< 3 \cdot 10^{-10}$  in the region of free motion (in the region, where the external perturbation is applied, this value was about 0.07, i.e. the method has worse precision in the region of perturbation, but further free motion is integrated precisely). As already mentioned, Noether's integrals of Appendix A separates in two conserved quantities  $P_\mu = P_\mu^{(x)} + P_\mu^{(y)}$ . Their conservation was satisfied in our numerical scheme (order  $n = 8$ ) with a precision of  $|\Delta P_0^{(x,y)}|/P_0 < 10^{-11}$ ,  $|\Delta \vec{P}^{(x,y)}|/P_0 < 10^{-13}$ . For total values in CMF we had  $|\vec{P}|/P_0 < 10^{-14}$ . For the angular momentum tensor we had found that its components have a cumulative numerical error, and for these values in the CMF we have an estimation  $|L_{0i}|/|L_{0i}^{(x)}|, |\Delta \vec{L}|/|\vec{L}| < 10^{-14} \cdot \text{num.of revolutions}$ , valid up to the maximal number of revolutions =  $10^6$  we considered.

The direct integration scheme is applicable upto  $v = 0.006$  ( $n = 8$ ). For greater velocities the solutions exhibit oscillations with time size comparable with the integration step, and rapidly increasing amplitude. The appearance of these oscillations is followed by violation of the conservation laws. This effect is caused by the increase of the light ladder step to a critical value, when it cannot be used anymore as a step of integration. The upper limit of  $v$  creates on fig.3c the right

limit of  $E$  (high velocity almost circular orbits) and lower limit of  $L$  (in this limit the trajectories are thin ellipses, and the particles come close to each other, reaching the upper limit of  $v$ ).

In the considered range of velocities the precession of the orbits is so slow, that the measurement of its angular frequency  $\omega_p = (\text{angle of precession})/(\text{time})$  requires special efforts. For this purpose we find intersections of the orbits with the circles  $r = \text{Const}$  and measure the difference of the angles  $\Delta\alpha_i$  for consecutive intersection points. For better precision we interpolate the solution between the integration points using the same high order polynomial of the integration method and find the intersection using dichotomy. Then we use large statistics of  $\Delta\alpha_i$  to find the average  $\Delta\alpha$ , which is related to the frequencies as  $\Delta\alpha = 2\pi(\omega_p/\omega_0)$ . Its mean-square error consists typically of about  $10^{-13}$  radians, leading to a relative error of  $(\omega_p/\omega_0)$  of about  $10^{-9}$ , sufficient for our purposes.

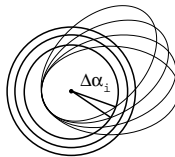


**Fig.10.** Measurement of precession rate.

Construction of the scatter plot fig.3: The four main input parameters of the program are the radius of the initial circular orbit and the 3 components of the external perturbation force. These were varied in a certain 4-dimensional region and 10,000 points were generated in the run. In 25% of cases the system was ionized (all these cases correspond to  $\sqrt{P^2} > 2m$ , i.e. when the external force gives the system enough energy for ionization). In 0.8% of the cases the particles were too close to each other and moved too fast and as a result, the algorithm lost applicability and diverged. These cases were rejected at earlier stages of the integration and did not consume much computation time. The remaining cases are displayed on fig.3.

To prove that the scatter plot occupies a 2-dimensional surface in the 4-dimensional space, we consider its sections by hypersurfaces  $EL^2 = \text{Const}$ . The projection of these sections on the plane  $(L, \Delta\omega_p/\omega_0)$  is shown on the inner image of fig.3b; projections to the planes  $(E, \Delta\omega_p/\omega_0)$  and  $(\omega_0, \Delta\omega_p/\omega_0)$  look similarly. As a result, we can conclude that the sections are 1-dimensional curves in a 4-dimensional space, which span a 2-dimensional surface with a change of the section parameter. Two other approaches to measure the dimension of the scatter plot are described in <sup>23</sup>: (1) computation of the Jacoby matrix for the mapping from the space of input parameters to the space of measured characteristics, and estimating its rank; (2) direct visualization of this 4-dimensional object by projection to the 3-dimensional space with color encoding of the 4th coordinate.

2. In the iterative scheme the initial segments of the trajectories  $\tau \in [0, 0.5]$  were set to circular orbits. To obtain non-circular orbits, we apply to both particles the local external forces  $-\vec{F}_{ext}$  and  $\vec{F}_{ext} + \Delta\vec{F}_{ext}$ . Such setting is convenient to control separately the orbits deviation from circular and asymmetry of initial conditions (the first one is controlled by  $\vec{F}_{ext}$ , the second by  $\Delta\vec{F}_{ext}$ ).

*Note:* There is still another type of the initial condition, where the data on initial segment are directly set to non-circular orbits. In principle, these two types of initial conditions are equivalent: the equations of motion are generally not satisfied on the initial segment, where the trajectories *are set* to arbitrary shapes, and non-zero right hand side of the equations in this segment play the role of an effective external force. However, concrete implementation of the non-circular initial condition creates certain problems in our scheme. The data on the initial segment should necessarily be presented in light ladder parametrization, for which the analytical representation is known only for the case of circular orbits. Moreover, the correct parametrization on the whole trajectory is recovered by further integration process from the initial segment, and its  $C^n$ -smoothness is guaranteed only if special conditions are satisfied (left and right derivatives upto  $n$ th order should coincide in a point  $\tau = 0.5$ ). For non-circular initial orbits the satisfaction of this property is problematic, while for circular orbits a global  $C^\infty$ -smooth parametrization can be easily constructed, and infinitely-differentiable external forces, used to control the shape of solution, preserve smoothness.

For convergence of the method the total number of light ladder steps  $Nls$  and the number of integration steps per light ladder step  $Nps$  should be set to  $Nps > 10^2$ ,  $Nls < 10$  at intermediate energies  $E \sim 1$  and to  $Nps > 10^3$ ,  $Nls < 5$  at high energies  $E \sim 3$ . Our stop-criterion of iteration

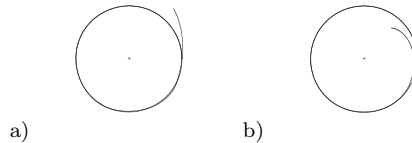
was  $\sum_i ((\vec{x}_n(\tau_i) - \vec{x}_{n-1}(\tau_i))^2 + (\vec{y}_n(\tau_i) - \vec{y}_{n-1}(\tau_i))^2) / (Nps * Nls) < \epsilon$ , where  $(\vec{x}_n, \vec{y}_n)$  represent the current iteration,  $(\vec{x}_{n-1}, \vec{y}_{n-1})$  – previous iteration, the sum is taken over all integration points, and  $\epsilon = 10^{-12}$ .

In the described simplest form the method can be applied up to velocities  $v = 0.8$  ( $E \sim 1$ ), then a stabilization is needed to keep it convergent. A stabilization procedure, proposed in <sup>16</sup>, suggests to combine the acceleration computed by the equations of motion with the acceleration stored from the previous iteration to  $\vec{a}_n(t) = 0.1\vec{a}_{eq}(t) + 0.9\vec{a}_{n-1}(t)$ , and integrate it to the trajectories of the current iteration. We have found that this type of stabilization, being applied to our problem at high energies, makes the method indifferently stable: it has no divergence but cannot reach the solution either. We have used another approach, based on the following predictor-corrector algorithm: We track the solution as a function of one control parameter  $\mu$  (which, for example, can be equal to initial velocity of the particles). The solutions found for the  $n$  previous values of  $\mu$  should be stored ( $n$  old copies of coordinate, velocity and acceleration arrays should be kept; while other variables, entering in the caching buffer, should not be copied). The dependence of the solution on  $\mu$  at each integration point is approximated by a polynomial of  $k$ th order using a least square method (in our implementation  $n = 10, k = 2$ ). This polynomial is used as a starting point for the iterations at a new value of the control parameter  $\mu + \Delta\mu$ . If the solution has a smooth dependence on the control parameter, this method produces a starting point placed much closer to the result than other types of initial guess. This fact considerably improves the convergence. The step  $\Delta\mu$  is chosen adaptively: decreased twice if convergence is lost and increased twice if the solution has been found, automatically keeping this value in the optimal region. This approach, earlier applied in <sup>1</sup> for the solution of 1D WF, accelerates the recovery of the solution along the  $\mu$ -axis by a factor of thousand, and keeps the method stable up to the velocity  $v = 0.98$ .

Other parameters, influencing the shape of solution, such as the components of the external force, in this method should be set to the given smooth functions of  $\mu$ , which should change from zero to (for example) certain constant values. Starting the procedure for circular orbits at the velocity  $v = 0.8$ , where the simplest scheme is convergent, we track one-dimensional families of solutions, corresponding to the given functions, and finally cover the whole space of input parameters in the region of convergence of the method. On fig.5 the right limit in  $E$ , bottom limit in  $\Delta L$  and upper limit in  $\eta^2$  are the limits of convergence of the method respectively at high energy, strong perturbation force  $F_{ext}$  and large asymmetry  $\Delta F_{ext}$ . The upper limit in  $\Delta L$ , close to the circular orbit, is related with a problem of another kind: Such solutions have very good convergence, but do not exhibit linear dependence in graphs  $\eta^2(E)$ , so that we cannot clearly separate symmetric and asymmetric phases by the described method.

An extra feature of the iterative scheme is the existence of artificial boundary effects, appearing near the end of the data arrays. Because at the end of the integration interval the future evolution is not known, the advanced Lorentz force should be omitted in this region. For the retarded Lorentz force we have used two possibilities: (a) single retarded Lorentz force or (b) double retarded Lorentz force is taken on the last step of the light ladder. Absence of the advanced force and various settings for retarded force lead to boundary effects, propagating to the inner regions of the integration interval. The amplitude of these effects is exponentially decreasing with the depth of penetration, so that the solution at several light ladder steps before the end of the integration is no more sensitive to boundary effects. It has also been found that boundary conditions of type (a) lead to stronger boundary effects, but support better convergence at higher energies than condition (b). Fig.11 shows the solutions, corresponding to boundary conditions of both types for value of velocity  $v = 0.86$ .

**Fig.11.** Two types of boundary effects in iterative scheme.



The described modification of the Lorentz force leads to non-conservation of the integrals of motion in the last step of light ladder. At the beginning of the trajectory in those regions, where the external forces are applied (and where the initial data are set – as we show above, this setting leads to the appearance of an effective external force) Noether's integrals are also not conserved.



On the remaining parts of the trajectory the conservation laws are valid, namely these parts are shown in the images fig.4. The conservation laws in these parts were satisfied with precision  $|\vec{P}|/P_0 < 10^{-10}$ ,  $|\Delta\vec{L}|/|\vec{L}| < 10^{-8}$ ,  $|L_{0i}|/|\vec{L}| < 10^{-7}$  at intermediate energies  $E \sim 1$ , slowly increasing upto  $|\vec{P}|/P_0, |\Delta\vec{L}|/|\vec{L}| < 10^{-6}$ ,  $|L_{0i}|/|\vec{L}| < 10^{-4}$  at high energies  $E \sim 3$ .

3. Computational time: most extensive computations are required for the construction of the scatter plot fig.3 (24 hours) and 3D graph fig.5 (120 hours). The computation was performed during one night, parallelly on 12 processors (300MHz MIPS R12000) of the GMD computer SGI/Onyx2.

## References

1. S. V. Klimenko, I. N. Nikitin, W. F. Urazmetov, *Int. J. Mod. Phys. C*, **10**, 905 (1999).
2. J. A. Wheeler and R. P. Feynman, *Rev. of Mod. Physics*, **17**, 157 (1945) and *Rev. of Mod. Phys.* **21**, 425 (1949).
3. K. Schwarzschild, *Göttinger Nachrichten*, 128,132 (1903), H. Tetrode, *Zeits. f. Physik* **10**, 137 (1922) and A. D. Fokker, *Zeits. f. Physik* **58**, 386 (1929).
4. A. Staruskiewicz, *Ann. Physik* **25**, 362 (1970).
5. J. L. Anderson, *Principles of Relativity Physics*, Academic press, New York 1967, p.225.
6. D. Leiter, *Am. J. Phys.* **38**, 207 (1970).
7. G. N. Plass, *PhD. Thesis*, Princeton University, 1946 (UMI dissertation services).
8. P. A. M. Dirac, *Proc. Roy. Soc. London* **167**, 148 (1938).
9. A. Einstein and W. Ritz, *Phys. Z* **10**, 323 (1909).
10. F. Hoyle and Jayant V Narlikar, *Cosmology and Action at a Distance Electrodynamics*, (World Scientific, Singapore 1996), see also F. Hoyle and J. V. Narlikar, *Rev. of Mod. Phys.* **67**, 113 (1995).
11. M. Schonberg, *Phys. Rev.* **69**, 211 (1946).
12. A. Schild, *Phys. Rev.* **131**, 2762 (1963) and *Science* **138**, 994 (1962).
13. C. M. Andersen and H. C. von Baeyer, *Phys. Rev. D* **5**, 2470 (1972).
14. R. D. Driver, *Phys. Rev. D* **19**, 1098 (1979), J. Hoag and R. D. Driver, *Nonlinear Analysis, Theory, Methods & Applications* **15**, 165 (1990).
15. S. V. Klimenko, I. N. Nikitin and W. F. Urazmetov, *Il Nuovo Cimento* **111**, 1281 (1998) and *Il Nuovo Cimento* **110**, 771 (1995).
16. C. M. Andersen and H. C. von Baeyer, *Phys. Rev. D* **5**, 802 (1972). The sign of the acceleration terms in equation 2.3 of this paper is wrongly calculated and this might affect the stability results.
17. R. A. Moore, D. W. Qi and T. C. Scott, *Can. J. Phys.* **70**, 772 (1992).
18. L. E. El'sgol'ts and S. B. Norkin, *Introduction to the Theory and Application of Differential Equations with Deviating Arguments*, (Academic Press, New York 1973).
19. C. G. Darwin, *Phil. Mag.* V.39, p.537 (1920).
20. J. De Luca, *Phys. Rev. E* **62**, 2060 (2000).
21. J. D. Jackson, *Classical Electrodynamics*, second edition, (John Wiley&Sons, New York 1975), p.657.
22. C.A.H. Paul, *Numerical Analysis Report No. 283*, Manchester Centre for Computational Mathematics (1995) (<http://www.ma.man.ac.uk/MCCM/MCCM.html>).
23. homepage of the project: <http://viswiz.gmd.de/~nikitin/wf/new/idea.html>